A Two-Species Model for Abnormal Tau Dynamics in Alzheimer's Disease

Zheyu Wen(✉), Ali Ghafouri, and George Biros

Oden Institute, University of Texas at Austin, 201 E. 24th Street, Austin, TX, USA
{zheyw,ghafouri}@utexas.edu, biros@oden.utexas.edu

Abstract. We construct image-driven, mechanism-based biomarkers for Alzheimer's disease (AD). These markers are parameters and predictions of a biophysical model of misfolded tau propagation, which is calibrated using positron emission tomography (PET) data. An example of such a model is the widely used single-species Fisher-Kolmogorov model (FK). In this article, we reveal a qualitative inconsistency between tau observations and the FK model predictions: FK has a bias towards maintaining the maximum misfolded tau to region of the initial misfolding, which most clinicians and modelers consider it to be the entorhinal cortex (EC). To partially address this EC bias, we introduce a simplified Heterodimer Fisher-Kolmogorov model (HFK) that tracks the dynamics of both abnormal and normal tau. To construct both FK and HFK models, we use a coarse, graph-based representation where nodes represent brain regions and edges represent inter-region connectivity computed using white matter tractography. The model parameters comprise migration, proliferation and clearance rates, which are estimated using a derivative-based optimization algorithm. We compare tau progression predictions between the FK and HFK models and conduct experiments using PET from 45 AD subjects. The HFK model achieved an average of 3.94% less relative fitting error compared to the FK model. Qualitatively, FK model overestimates misfolded tau in EC while HFK does not.

Keywords: Alzheimer tau propagation · Inverse problem · Graph-based representation

1 Introduction

Two prevailing factors in the progression of AD are the progression of misfolding of the amyloid-β and tau protein. Here, we just focus on the misfolded or abnormal tau protein, which is particularly toxic, hindering the proper function of the nervous system and leading to atrophy, necrosis, and ultimately causing death [1,2]. Quantifying the spatio-temporal dynamics of misfolded tau holds the promise of helping understand AD dynamics and generating biomarkers for clinical management. Image-driven biophysical biomarkers have the potential to

Supplementary Information The online version contains supplementary material available at https://doi.org/10.1007/978-3-031-47425-5_7.

J. Woo et al. (Eds.): MICCAI 2023 Workshops, LNCS 14394, pp. 69–79, 2023.
https://doi.org/10.1007/978-3-031-47425-5_7

help with disease staging and subject stratification [10]. Misfolded tau spreading depends on the initial brain misfolding locations and the rate at which the misfolding amplifies and spreads. Tau aggregates are believed to initiate misfolding in the entorhinal cortex (EC), and primarily invade healthy proteins along neuronal pathways [3,4]. Longitudinal PET scans using F-AV-1451 tracer (tauvid) can image the spread of tau protein. The most commonly used mathematical model for tau progression is the FK model [5,6,15,16]. This model requires the initial state of tau protein and three parameters to describe the migration, proliferation and clearance of tau. However, even qualitatively, the model predicts the highest tau abnormality in regions other than the ones observed in PET scans. This behavior is due to the monotonic property of FK model, which means that the spatial location of the maximum tau does not change and remains the same as the seeding location. This is inconsistent to observed data. We report this inconsistency in Fig. 3 using clinical PET images from Alzheimer's Disease Neuroimaging Initiative (ADNI) [7]. The maximum in the image is not in EC and in some cases it is far from that region.

Contributions: We propose a two-species model, which we term Heterodimer Fisher-Kolmogorov model (HFK) to represent the normal tau (healthy and non-observable) and abnormal tau (observable) progression in AD patients. Our model takes into account the migration, proliferation and clearance of abnormal tau but also its coupling with the normal tau protein. In this context our contributions are the following: (i) We show the monotonic property of FK model both in a synthetic test and clinical results. (ii) We propose the HFK graph model that considers both healthy and unhealthy tau protein. (iii) We propose an inversion algorithm for reconstructing the model parameters. (iv) We test our algorithm on all AD clinical tau PET scans and compare the FK model with the HFK model.

Related Work: FK has been widely studied at different scales in studying protein misfolding in the brain, from molecular level models [11,12] to kinetic equations [9,13,14] and graph models like ours [15–18]. These studies integrated biophysical FK models with MRI and PET data (like us) and relate the initial misfolding location (the seed) and different parameter values to different prion-like diseases, including AD. In AD models, the standard tau seeding location is the EC region. Once biophysical parameters are computed, they are combined with other imaging features for downstream clinical tasks.

There is also work with more complex multi-species AD models [10,19,31] that are similar to our HFK model. In [19], the authors formulate the AD modeling using a two-species framework, and in [10], the authors assume that the healthy tau values are much higher than the abnormal tau and derive the single-species FK model. In all multi-species studies analyze the problem qualitatively and, to our knowledge, they have not fitted these multispecies models to clinical data. Our work aims to provide a first study that does so and compares it with the popular single-species FK model.

2 Methodology

Let $\mathcal{B} \subset \mathbb{R}^3$ be the brain domain and let $\mathbf{x} \in \mathcal{B}$ denote a point. Let $c_a(\mathbf{x}, t)$ denote the abnormal tau, where t represents time from the onset of the disease. To model the spread of abnormal tau in the brain, we first coarsen in space and adopt a graph-based approach that has been widely used in literature [15,16,18]. Specifically, we define a graph $\mathcal{G}$ using a standard parcellation of $\mathcal{B}$. The graph is composed of a set of N vertices, which represents a collection of N regions of interest (ROI) defined in an atlas. Each vertex corresponds to a parcel. The edges between vertices are undirected and their weights $\mathbf{w}$ indicate the white-matter connectivity strength between parcels, from tractography and diffusion tensor imaging. Given the tractography-computed parcel connectivity matrix $\mathbf{D}$ [30], the Laplacian $\mathbf{L}$ is defined by $\mathbf{L} = \text{diag}\left(\sum_{j=1}^{N}[\mathbf{D}(\mathbf{w})]_{ij}\right) - \mathbf{D}(\mathbf{w})$ [20]. We define the set of abnormal tau for all the nodes as $\mathbf{c}_a(t)$ where $c_a^i(t) \in [0, 1]$ represents the abnormal tau at the i^{th} parcel. In order to quantify the level of tau abnormality, we compare the statistical distribution of Tau-PET intensity in gray matter regions with distribution in the cerebellum. To compare these distributions, we employ the Maximum Mean Discrepancy (MMD) metric [24], where we denote μ_i as the MMD score for the i^{th} parcel. Additionally, we normalize the MMD score by defining $c_a^i = 1 - e^{-\mu_i \sigma}$, where σ is a hyperparameter; we select $\sigma = 0.3$ that give the best fit in the inversion. FK and HFK model the tau dynamics at the parcel resolution. They're defined as follows.

Single-species FK Model: The Fisher-Kolmogorov model [5,6,32] is given by

$$\frac{\partial \mathbf{c}_a}{\partial t} = -\kappa \mathbf{L}\mathbf{c}_a + \rho \mathbf{c}_a \odot (\mathbf{1} - \mathbf{c}_a) - \gamma \mathbf{c}_a, \tag{1a}$$

$$\mathbf{c}_a(0) = \mathbf{p}_0. \tag{1b}$$

FK involves three terms: diffusion, reaction and clearance. The diffusion term is defined by $-\kappa \mathbf{L}\mathbf{c}_a$ and $\kappa \in \mathbb{R}^+$ is the diffusion coefficient or migration rate. It captures the spatial spreading. The reaction term is defined by $\rho \mathbf{c}_a \odot (\mathbf{1} - \mathbf{c}_a)$ where $\odot$ is the Hadamard elementwise vector product, and $\rho \in \mathbb{R}^+$ is the proliferation coefficient. Reaction represents growth of abnormal tau within the region. Finally, we define a clearance term as $-\gamma \mathbf{c}_a$ to describe the abnormal protein removal, and $\gamma \in \mathbb{R}^+$ is a clearance coefficient. $\mathbf{p}_0$ is the parametrization of the initial condition $\mathbf{c}_a(0)$. Here, following the current clinical consensus, we fix it at the EC region to be one and zero elsewhere. The time horizon for Eq. (1) is set to one. Using non-dimensional analysis, the change of the time horizon corresponds to just scaling of the model parameters [8]. As we discussed, the FK model is widely used in describing tau propagation but it does not allow the location of maximum tau to change.

Two-species HFK Model: To address this FK limitation, we introduce dynamics for the *normal* tau protein $\mathbf{c}_n$ and we modify the reaction term in

Eq. (1). The HFK model is given by the following ODE system.

$$\frac{\partial \mathbf{c}_a}{\partial t} = -\kappa \mathbf{L}\mathbf{c}_a + \rho \mathbf{c}_a \odot \mathbf{c}_n - \gamma \mathbf{c}_a, \tag{2a}$$

$$\frac{\partial \mathbf{c}_n}{\partial t} = -\rho \mathbf{c}_a \odot \mathbf{c}_n, \tag{2b}$$

$$\mathbf{c}_a(0) = \mathbf{p}_0,\ \mathbf{c}_n(0) = \mathbf{1} - \mathbf{p}_0. \tag{2c}$$

Here $\kappa, \rho, \gamma, \mathbf{p}_0$ are defined as in Eq. (1). The time horizon is set to one. Again $\mathbf{p}_0$ is fixed to be one at EC and zero elsewhere. We assume there is no diffusion and clearance for normal tau. Notice that since $\mathbf{c}_n = 0$ at EC at all times, $\mathbf{c}_a$ at EC can only spread and never grow. This minimal change allows the location of maximum tau to temporally change, without introducing any new model parameters.

Parameter Estimation: We aim to estimate the migration κ, proliferation ρ and clearance γ coefficients given the PET data $\mathbf{d}$ (normalized MMD scores). The optimization problem, for the HFK case, is given by

$$\min_{\kappa,\rho,\gamma} J \coloneqq \frac{1}{2}\|\mathbf{c}_a(1) - \mathbf{d}\|_2^2$$
$$\text{subject to } \begin{cases} \frac{\partial \mathbf{c}_a}{\partial t} = -\kappa \mathbf{L}\mathbf{c}_a + \rho \mathbf{c}_a \odot \mathbf{c}_n - \gamma \mathbf{c}_a, \\ \frac{\partial \mathbf{c}_n}{\partial t} = -\rho \mathbf{c}_a \odot \mathbf{c}_n, \\ \mathbf{c}_a(0) = \mathbf{p}_0, \\ \mathbf{c}_n(0) = \mathbf{1} - \mathbf{p}_0, \\ \kappa,\ \rho,\ \gamma \geq 0. \end{cases} \tag{3}$$

where $\mathbf{d}$ is the PET subject tau abnormality for all parcels. To solve this constrained optimization problem, we introduce adjoint variables $\mathbf{a}_a$ and $\mathbf{a}_n$ and form the Lagrangian $\mathcal{L}$ [33]. Taking variations w.r.t the adjoints recovers Eq. (2). Taking variations w.r.t to $\mathbf{c}_a$ and $\mathbf{c}_n$ leads to the adjoint equations $\frac{\partial \mathbf{a}_a}{\partial t} = \kappa \mathbf{L}^\intercal \mathbf{a}_a + \rho \mathbf{c}_n \odot (\mathbf{a}_n - \mathbf{a}_a) + \gamma \mathbf{a}_a$, $\frac{\partial \mathbf{a}_n}{\partial t} = \rho \mathbf{c}_a \odot (\mathbf{a}_n - \mathbf{a}_a)$, $\mathbf{a}_a(1) = \mathbf{d} - \mathbf{c}_a(1)$, $\mathbf{a}_n(1) = \mathbf{0}$. Taking variations w.r.t the model parameters give the gradient equations $\frac{\partial \mathcal{L}}{\partial \kappa} = \int_0^1 \mathbf{a}_a^\intercal(\mathbf{L}\mathbf{c}_a)dt$, $\frac{\partial \mathcal{L}}{\partial \rho} = \int_0^1 (\mathbf{a}_n - \mathbf{a}_a)^\intercal \mathbf{c}_a \odot \mathbf{c}_n dt$ and $\frac{\partial \mathcal{L}}{\partial \gamma} = \int_0^1 \mathbf{a}_a^\intercal \mathbf{c}_a dt$. To evaluate the derivative of J w.r.t the parameters, we first solve Eq. (2) to get $\mathbf{c}_a(t), \mathbf{c}_n(t)$, then we solve the adjoint equations backward in time for $\mathbf{a}_n(t), \mathbf{a}_a(t)$, and finally we plug these values to the gradient.

Numerical Scheme: We use the LSODA ODE solver [26]. The parameters $\kappa,\ \rho,\ \gamma \in [0, \infty]$. We set the initial guess $\kappa = 0,\ \rho = 0,\ \gamma = 0$. The optimization problem is solved using a reduced gradient L-BFGS solver [21]. The optimizer stops when the gradients are below tolerance 1E−3. It turns out that the inversion is not sensitive to the initial guess.

3 Results

We evaluate the new model by answering the following two questions:

(Q1) How do the dynamics of the HFK and FK differ?
(Q2) How well can HFK and FK fit clinical scans?

We discuss the first point using synthetic simulations. We provide preliminary results for the second question using all AD scans from ADNI. We evaluate our results both qualitatively and quantitatively.

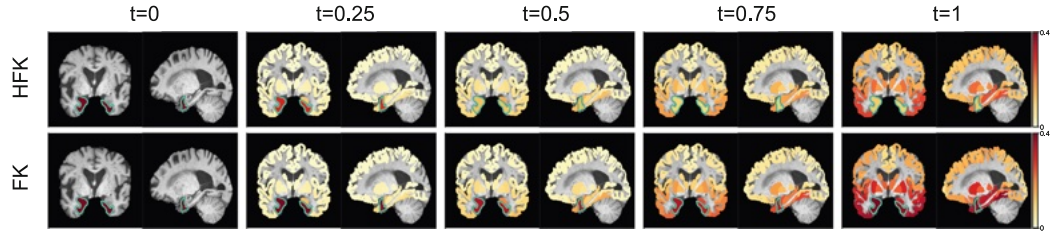

Fig. 1. Spatiotemporal progression of tau using HFK and FK models. Given the same initial tau seed and model parameters for both models, we show the propagation of tau over time (from left to right). The top row are results from HFK model. Results from FK are shown in the bottom row. The EC parcel is highlighted by blue solid contour lines. (Color figure online)

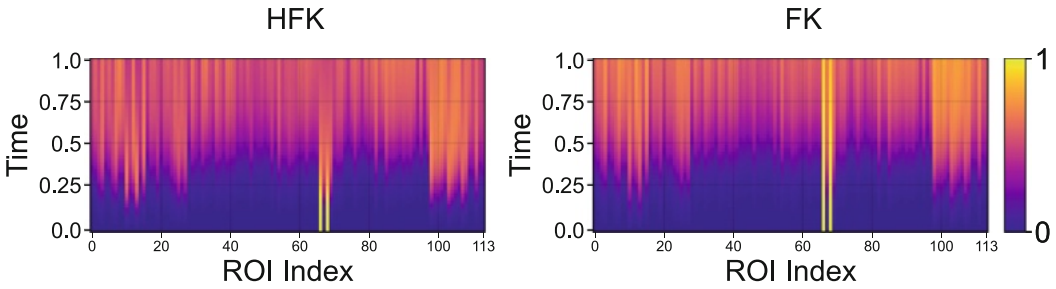

Fig. 2. Average spatio-temporal dynamics of tau propagation for HFK and FK forward model. Given the same initial seed located at the EC parcel, we feed the HFK and FK model with 1000 sets of parameters, and *average* the ODE solution at $t \in [0, T]$ across all parameter sets. X-axis represents parcels in the brain under MUSE template (space information), and Y-axis presents 50 uniformly-spaced time points in $t \in [0, 1]$. The two bright lines correspond to the EC parcels. HFK and FK perform qualitatively differently, as in the majority of cases the maximum misfolding is in the EC region for FK; but not for HFK.

(Q1) Synthetic Simulations: To illustrate the model differences, we generate data using Eq. (1) and Eq. (2) and $\kappa = 4,\ \rho = 5,\ \gamma = 1$. The initial misfolding is placed at the left and right EC parcels. The simulation time horizon is set to one and we sample five time snapshots at $t = 0,\ 0.25,\ 0.5,\ 0.75,\ 1$. We show the results in Fig. 1. Notice the significant differences in EC $\mathbf{c}_a(t)$ for $t \geq 0.5$.

The FK model maintains the EC to be the maximum whereas HFK does not. Again, at time $t = 1$, EC remains the region with maximum $\mathbf{c}_a$ in FK whereas in HFK other regions have higher $\mathbf{c}_a$. Qualitatively, the HFK dynamics better align with the clinical Tau-PET data.

We repeat these simulations for 1000 sets of parameters, and record the average spatio-temporal dynamics for both models over all sets of parameters. We sample uniformly from $\kappa \in [0, 10]$, $\rho \in [0, 20]$ and $\gamma \in [0, 5]$ for both models. The range of parameters are chosen since the ODE solution from them represent the patterns observed in clinical data. In addition, the inverted parameters lies in these ranges, which makes the choice reasonable. The FK-maximum remains at the EC parcels (the two bright lines in Fig. 1), whereas this is not the case for the HFK model.

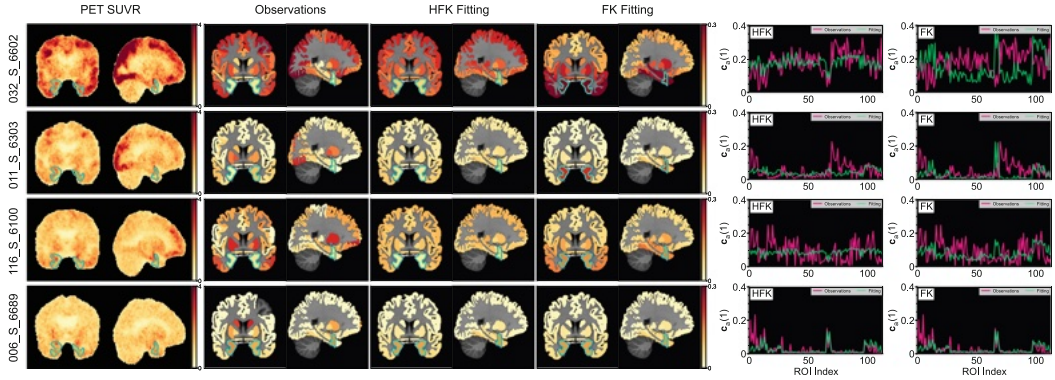

Fig. 3. Model calibration for four AD subjects from ADNI. Each row corresponds to a subject. From left to right in each panel we show the PET abnormal tau, processed regional abnormal tau MMD, the HFK fit, and the FK fit. The 1D curves show the HFK and FK fits as a function of the parcel id (ROI Index). In the 2D images, the EC region is highlighted by a solid contour line.

Table 1. Inversion results for four ADNI subjects using the FK and HFK models. $e_{\mathbf{d},\ell_1}$ and $e_{\mathbf{d},\ell_2}$ (or $\sqrt{2J}/\|\mathbf{d}\|_2$ from Eq. (3)) are relative fitting errors in ℓ_1 and ℓ_2 norms separately. κ, ρ and γ are estimated parameters from each model. For each subject, better fitting with lower errors are in bold.

SubjectId	HFK					FK				
	$e_{\mathbf{d},\ell_2}$	$e_{\mathbf{d},\ell_1}$	κ	ρ	γ	$e_{\mathbf{d},\ell_2}$	$e_{\mathbf{d},\ell_1}$	κ	ρ	γ
032_S_6602	**3.39E−1**	**2.83E−1**	9.86	9.34	3.63	6.78E−1	6.21E−1	4.06	3.68	2.34E−1
011_S_6303	**6.88E−1**	**6.54E−1**	5.58	2.06	1.29E−1	9.10E−1	8.44E−1	2.10	1.94	7.52E−1
116_S_6100	**5.69E−1**	**5.59E−1**	6.72	8.71	4.55	6.31E−1	6.23E−1	5.36	2.93	3.79E−1
006_S_6689	6.96E−1	**6.00E−1**	2.40	1.01	0	**6.94E−1**	6.29E−1	3.10	1.30	2.64E−1

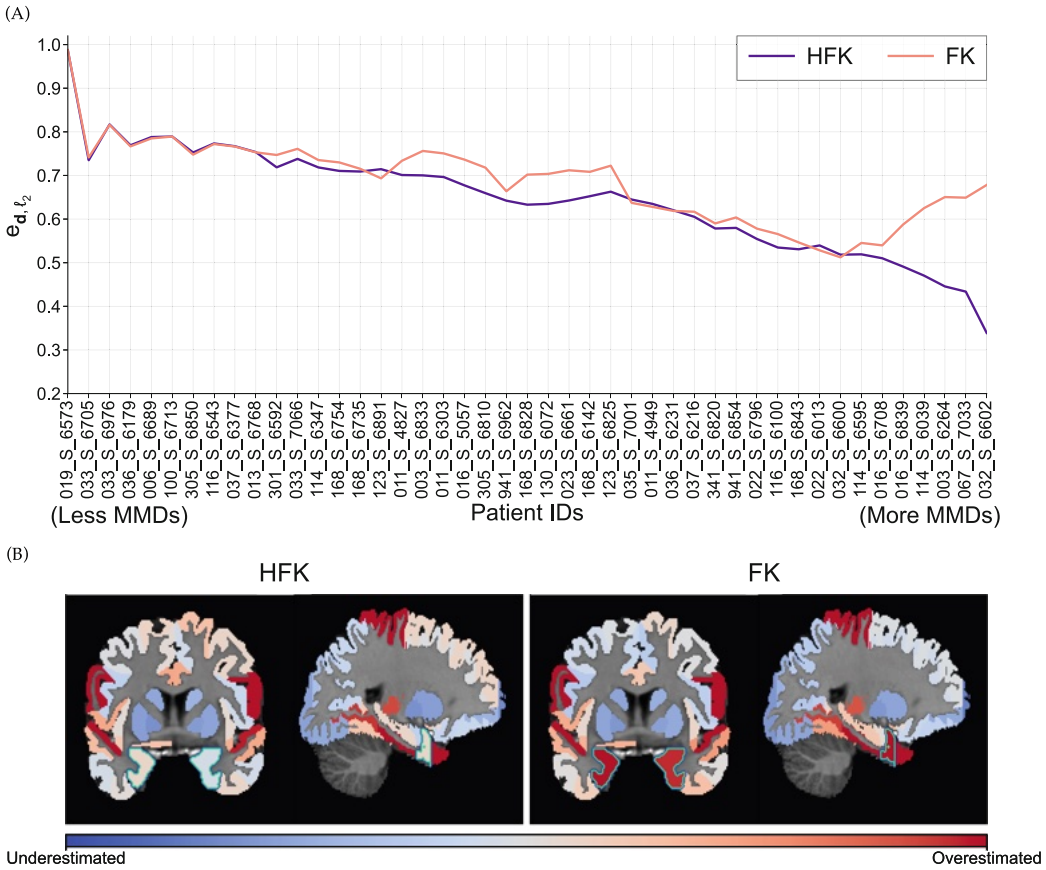

Fig. 4. Evaluation on 45 ADNI AD subjects. (A) ℓ_2 misfit error for FK and HFK (two-subject moving average). The subjects are sorted by total MMD scores (sum over regions). HFK does slightly better but both models struggle especially for subjects with high MMD. (B) Over- and underestimated regions for HFK and FK models. We average the fitting result for each region over all subjects and compare with averaged MMD data. The over- or underestimation for each region is determined by the relative difference between fitting and observation. FK model consistently overestimates the EC region while HFK not

(Q2) Clinical PET Data: We use preprocessed MRI and PET images downloaded from ADNI [7]. Although many subjects have several PET time snapshots available, in this study we only use one of them. (Using more time snapshots is part of ongoing work.) In total, we have 45 AD subjects, 19 of them are female and 26 are male with age mean(std) is 74.95(8.87). The acquisition time spans from 09/07/2017 to 05/17/2022. We follow the preprocessing workflow from [16]. For each subject, affine registration is performed for the T1 image of each subject to healthy brain template using FSL [22]. The subject's image is then parcellated using the MUSE template [23]. PET images are intensity-normalized by the median in the gray matter of cerebellum, which results in Standard Uptake Value Ratio (SUVR). The SUVR values are quite noisy. As discussed above, we define the regional tau abnormality with MMD [24]. As most ADNI patients

don't have DTI data, we use 20 Diffusion Tensor Imaging (DTI) scans obtained from the Harvard Aging Brain Study (HABS) [25] to generate 20 connectivity matrices $\mathbf{D}$ using the MRtrix3 software [30]. Throughout all experiments, we consistently utilize the same connectivity matrix, which is obtained by first averaging the connectivity matrices from the 20 DTI images from HABS and then forming the graph Laplacian.

We present our algorithm's performance qualitatively on four clinical scans and quantitatively on all AD subjects from the ADNI dataset. The regional (or per parcel) observed abnormal tau $\mathbf{d}$ is computed by the Tau-PET images described above. We aim to estimate migration, proliferation and clearance coefficients for both models separately. Qualitative evaluations are present in Fig. 3. For each patient, the figure shows its Tau-PET image, parcellated tau MMD data, and inversion results from HFK and FK models. The Tau-PET scans and observations in the first three subjects do not have high tau values in EC. The FK model tries to fit the observed data but it is qualitatively off. Both models do well in the last patient as the highest c_a value is at the EC parcel. This illustrates that HFK is also capable to maintain a high EC tau value if needed. (See supplementary for tau progression videos.) We report the fit errors in Table 1. The HFK model performs slightly better but both models struggle. The results point to the need for a richer parametrization or different models. For example, what if the widely accepted assumption of the EC region being the tau misfolding origination is not correct? Previous studies in the literature have identified the necessity to address this [34].

The aforementioned phenomenon exists consistently in the AD dataset. Figure 4(A) shows the overall performance across all AD patients data. The patients are sorted by their summation of MMD in all regions, lower to higher. In this sense the tau abnormality signal is stronger from left to right. For each subject we report the relative ℓ_2 norm error. HFK achieves 3.94% better relative error in ℓ_2 norm over FK. Furthermore, to visualize the estimation error of FK model on EC region, we present a qualitative evaluation in Fig. 4(B). We average the fitting results for each parcel over patients, and compare with averaged observation MMD data. The under- or overestimation is computed according to the relative difference between regional fitting and regional MMD data. The significant difference lies in EC region between HFK and FK models.

4 Conclusions

We presented HFK, a simple model (in terms of number of free parameters) to describe the abnormal tau propagation in the brain. Our main point is that the commonly used FK model is inconsistent with the observed tau data. Similarly to FK, HFK captures migration, proliferation, and clearance of the abnormal tau in a graph model, but in addition introduces dynamics for the normal tau. The HFK has a *a qualitatively different* behavior and matches the observed data better. We also presented an observation model using MMD and a reconstruction algorithm to estimate migration, proliferation and clearance coefficients of the model based

on the observation. We tested the two models on both synthetic and clinical data. From the performance averaged over all AD patients, FK consistently overestimates EC regions. Without increasing the number of model parameters, we improved the model performance. Specifically, when the maximum signal in PET does not lie in EC region, the HFK model outperforms the FK one.

The results however show that both models struggle to fit the data. A possible reason that our assumption of placing the tau abnormality origination at the entorhinal cortex. A potential solution may take initial condition as an additional variable to optimize and apply ℓ_0 or ℓ_1 constraints. Future work includes relaxing this assumption and inverting for the initial condition in Eq. (2), as well as conducting sensitivity studies on the parcellation and tractography algorithms. In the supplementary material, we provide a video demonstrating the fitting results obtained using the exhaustively searched IC. Two other directions in increasing the biophysical model fidelity is coupling to the gray matter atrophy and to amyloid-β dynamics.

References

1. Sintini, I., et al.: Longitudinal tau-pet uptake and atrophy in atypical Alzheimer's disease. NeuroImage: Clin. **23**, 101823 (2019)
2. Bucci, M., Chiotis, K., Nordberg, A.: Alzheimer's disease profiled by fluid and imaging markers: tau pet best predicts cognitive decline. Molecul. Psychiat. **26**(10), 5888–5898 (2021)
3. Braak, H., Del Tredici, K.: The preclinical phase of the pathological process underlying sporadic alzheimer's disease. Brain **138**(10), 2814–2833 (2015)
4. Braak, H., Braak, E.: Neuropathological stageing of Alzheimer-related changes. Acta Neuropathol. **82**(4), 239–259 (1991)
5. Fisher, R.A.: The wave of advance of advantageous genes. Annal. Eugen. **7**(4), 355–369 (1937)
6. Kolmogorov, A.N.: A study of the equation of diffusion with increase in the quantity of matter, and its application to a biological problem. Moscow Univ. Bull. Math. **1**, 1–25 (1937)
7. Petersen, R.C., et al.: Alzheimer's disease neuroimaging initiative (ADNI): clinical characterization. Neurology **74**(3), 201–209 (2010). http://adni.loni.usc.edu/
8. Subramanian, S., Scheufele, K., Mehl, M., Biros, G.: Where did the tumor start? An inverse solver with sparse localization for tumor growth models. Inverse Probl. **36**(4), 045006 (2020)
9. Scheufele, K., Subramanian, S., Biros, G.: Calibration of biophysical models for tau-protein spreading in Alzheimer's disease from pet-MRI. arXiv preprint arXiv: 2007.01236 (2020)
10. Fornari, S., Schäfer, A., Jucker, M., Goriely, A., Kuhl, E.: Prion-like spreading of Alzheimer's disease within the brain's connectome. J. Roy. Soc. Interf. **16**(159), 20190356 (2019)

11. Cohen, F.E., Pan, K.M., Huang, Z., Baldwin, M., Fletterick, R.J., Prusiner, S.B.: Structural clues to prion replication. Science **264**(5158), 530–531 (1994)
12. Jarrett, J.T., Lansbury, P.T., Jr.: Seeding "one-dimensional crystallization" of amyloid: a pathogenic mechanism in Alzheimer's disease and scrapie? Cell **73**(6), 1055–1058 (1993)
13. Bertsch, M., Franchi, B., Marcello, N., Tesi, M.C., Tosin, A.: Alzheimer's disease: a mathematical model for onset and progression. Math. Med. Biol. J. IMA **34**(2), 193–214 (2017)
14. Weickenmeier, J., Kuhl, E., Goriely, A.: Multiphysics of prionlike diseases: progression and atrophy. Phys. Rev. Lett. **121**(15), 158101 (2018)
15. Schäfer, A., Peirlinck, M., Linka, K., Kuhl, E.: Alzheimer's Disease Neuroimaging Initiative (ADNI): Bayesian physics-based modeling of tau propagation in Alzheimer's disease. Front. Physiol. **12**, 702975 (2021)
16. Vogel, J.W., et al.: Spread of pathological tau proteins through communicating neurons in human Alzheimer's disease. Nat. Commun. **11**(1), 2612 (2020)
17. Garbarino, S., Marco, L.: Alzheimer's Disease Neuroimaging Initiative: Investigating hypotheses of neurodegeneration by learning dynamical systems of protein propagation in the brain. Neuroimage **235**, 117980 (2021)
18. Kim, H.R., et al.: Comparison of Amyloid beta and tau spread models in Alzheimer's disease. Cereb. Cortex **29**(10), 4291–4302 (2019)
19. Matthäus, F.: Diffusion versus network models as descriptions for the spread of prion diseases in the brain. J. Theor. Biol. **240**(1), 104–113 (2006)
20. Chung, F.R.: Spectral Graph Theory, Chapter 1. American Mathematical Society (1997)
21. Zhu, C., Byrd, R.H., Lu, P., Nocedal, J.: Algorithm 778: L-BFGS-B: Fortran subroutines for large-scale bound-constrained optimization. ACM Trans. Math. Softw. **23**(4), 550–560 (1997)
22. Smith, S.M., et al.: Advances in functional and structural MR image analysis and implementation as FSL. Neuroimage **23**, S208–S219 (2004)
23. Doshi, J., Erus, G., Ou, Y., Resnick, S.M., Gur, R.C., Gur, R.E.: Alzheimer's Neuroimaging Initiative: MUSE: MUlti-atlas region Segmentation utilizing Ensembles of registration algorithms and parameters, and locally optimal atlas selection. Neuroimage **127**, 186–195 (2016)
24. Gretton, A., Borgwardt, K.M., Rasch, M.J., Schölkopf, B., Smola, A.: A kernel two-sample test. J. Mach. Learn. Res. **13**(1), 723–773 (2012)
25. Dagley, A., et al.: Harvard aging brain study: dataset and accessibility. Neuroimage **144**, 255–258 (2017). https://habs.mgh.harvard.edu/
26. Petzold, L.: Automatic selection of methods for solving stiff and nonstiff systems of ordinary differential equations. SIAM J. Sci. Satist. Comput. **4**(1), 136–148 (1983)
27. Morey, R.D., Romeijn, J.-W., Rouder, J.N.: The philosophy of Bayes factors and the quantification of statistical evidence. J. Math. Psychol. **72**, 6–18 (2016)
28. Spiegelhalter, D.J., Best, N.G., Carlin, B.P., Van Der Linde, A.: Bayesian measures of model complexity and fit. J. Roy. Stat. Soc. Ser. B (Stat. Methodol.) **64**(4), 583–639 (2002)
29. Stoica, P., Selen, Y.: Model-order selection: a review of information criterion rules. IEEE Signal Process. Magaz. **21**(4), 36–47 (2004)
30. Tournier, J.-D., et al.: MRtrix3: a fast, flexible and open software framework for medical image processing and visualisation. Neuroimage **202**, 116–137 (2019)
31. Weickenmeier, J., et al.: A physics-based model explains the prion-like features of neurodegeneration in Alzheimer's disease, Parkinson's disease, and amyotrophic lateral sclerosis. J. Mech. Phys. Solids **124**, 264–281 (2019)

32. Iturria-Medina, Y., et al.: Epidemic spreading model to characterize misfolded proteins propagation in aging and associated neurodegenerative disorders. PLoS Comput. Biol. **10**(11) (2014)
33. Tröltzsch, F.: Optimal control of partial differential equations: theory, methods, and applications. Am. Math. Soc. **112** (2010)
34. Vogel, J.W., et al.: Four distinct trajectories of tau deposition identified in Alzheimer's disease. Nat. Med. **27**(5), 871–881 (2021)